

# Efficient Concertormer for Image Deblurring and Beyond

Pin-Hung Kuo

Jinshan Pan

Shao-Yi Chien

Ming-Hsaun Yang

## Abstract

The Transformer architecture has achieved remarkable success in natural language processing and high-level vision tasks over the past few years. However, the inherent complexity of self-attention is quadratic to the size of the image, leading to unaffordable computational costs for high-resolution vision tasks. In this paper, we introduce Concertormer, featuring a novel Concerto Self-Attention (CSA) mechanism designed for image deblurring. The proposed CSA divides self-attention into two distinct components: one emphasizes generally global and another concentrates on specifically local correspondence. By retaining partial information in additional dimensions independent from the self-attention calculations, our method effectively captures global contextual representations with complexity linear to the image size. To effectively leverage the additional dimensions, we present a Cross-Dimensional Communication module, which linearly combines attention maps and thus enhances expressiveness. Moreover, we amalgamate the two-staged Transformer design into a single stage using the proposed gated-dconv MLP architecture. While our primary objective is single-image motion deblurring, extensive quantitative and qualitative evaluations demonstrate that our approach performs favorably against the state-of-the-art methods in other tasks, such as deraining and deblurring with JPEG artifacts. The source codes and trained models will be made available to the public.

## 1. Introduction

In recent years, deep learning has driven significant advances in image restoration, with deep convolutional neural networks (CNNs) becoming widely used for image deblurring. The core operation in CNNs, i.e., convolution, is effective for extracting local features but limited in capturing non-local features, which are essential for deblurring.

The self-attention (SA) mechanism, on the other hand, excels at capturing non-local information and has shown promising results in image deblurring [8]. However, the high computational costs make it challenging to apply, particularly to high-resolution images.

Window-based multi-head self-attention (W-MSA) [37,

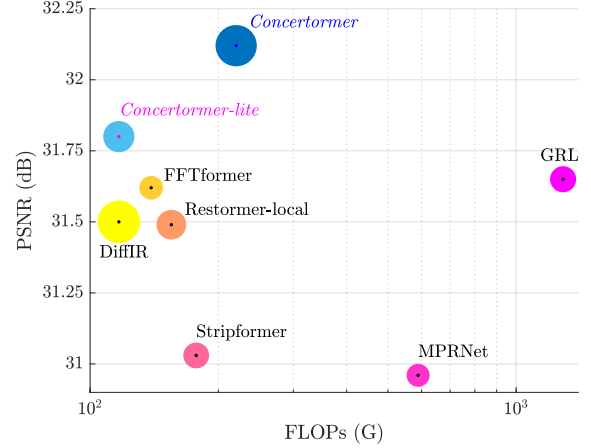


Figure 1. PSNR vs FLOPs on the HIDE [57] dataset. Our models are marked in blue and magenta text. The area of circles is proportional to the number of parameters.

[67] mitigates computational costs by limiting the calculation area. However, this approach suffers from limited receptive fields, making it less effective for capturing global relationships. As illustrated in Fig. 2(c), W-MSA processes each block in the input feature map independently. Although the shifted window technique communicates attention between neighboring blocks, it requires a sufficient number of blocks to model global relationships effectively.

Transposed SA is an alternative approach, as used in Restormer [82], which calculates self-attention along the channel dimension instead of the spatial dimension. However, this approach underestimates the importance of local connectivity. As shown in Fig. 2(d), transposed self-attention loses spatial connectivity during matrix multiplication: random column permutations in  $\mathbf{Q}$  and  $\mathbf{K}$  do not affect the result, meaning that transposed SA scarcely retains spatial connectivity information.

To address the aforementioned problems, we propose an efficient Transformer of Concerto Self-Attention, i.e., *Concertormer*, specifically for image deblurring. This model simultaneously captures both local and global connectivity with a lower computational cost. By dividing feature maps into grids and a specific number of heads, Concerto Self-Attention introduces an additional dimension compared to

the typical multi-head self-attention mechanism. To utilize this additional dimension along with the attention heads, we introduce a learnable linear projection mechanism, termed *Cross-Dimensional Communication*, which enables aggregation across independent attention maps.

The CSA is an efficient framework for self-attention calculation, which is adaptable to existing methods, such as transposed SA for image restoration. Notably, the computational complexity of this self-attention mechanism scales linearly with image size (Section 4.1).

Another key component of Transformer models is the feed-forward network (FFN), which functions as a key-value memory mechanism [20] and is essential for contextualization [30]. This has led to the widespread use of a two-stage architecture, i.e., self-attention followed by an FFN, in NLP applications. Although the FFN’s role in enhancing feature representation is well-established in NLP, its effectiveness in vision tasks remains uncertain. Moreover, the conventional two-stage Transformer architecture limits design flexibility. To address this, we introduce the gated-dconv MLP (gdMLP), an adaptation of the gated MLP [39] with depth-wise convolution and without layer normalization, condensing the two-stage structure into a single stage and reducing model complexity.

The main contributions of this work are as follows:

- We propose *Concerto Self-Attention*, an approach that effectively models both global and local features across spatial and channel domains with linear complexity.
- Leveraging the additional dimensions provided by Concerto Self-Attention, we introduce a Cross-Dimensional Communication module that linearly combines independent attention maps, enhancing feature exploration for improved image restoration.
- We develop a streamlined gdMLP module, which simplifies the original FFN in Transformers, thereby enhancing architectural flexibility and expressive ability.

We evaluate the proposed method on image deblurring datasets, demonstrating its favorable performance against state-of-the-art approaches. Additionally, we show that it is versatile, effectively extending to other image restoration tasks like deraining and deblurring with JPEG artifacts.

## 2. Related Work

**Image Deblurring.** Traditionally, blind image deblurring has relied on developing image priors. Inspired by dehazing methods [24], the dark channel prior proved effective for deblurring [49]. Since then, various priors have been proposed, including the hyper-Laplacian prior [48], extreme channels prior [72], graph-based image prior [5], local maximum gradient prior [9], and sparsity-based methods [10]. Recently, CNNs [4, 33, 80, 88, 89] have outperformed conventional priors in image restoration tasks. Multi-scale de-

sign became popular in computer vision [23, 26, 33, 34, 50, 73] and was soon adopted for deblurring. Nah et al. [46] introduced a multi-scale model with residual blocks [25]. Following U-Net’s success in segmentation [55], researchers adopted this architecture for deblurring, utilizing its hierarchical structure to explore cross-scale relationships [2, 12, 13, 32, 61, 81, 83, 87]. Tao et al. [61] refined this multi-scale design by integrating U-Nets with LSTMs as latent layers, while Zhang et al. [83] proposed a multi-patch network where each U-Net processes differently sized patches, inspiring further work [81].

Rather than using cascaded U-Nets for different resolutions or patches, Cho et al. [13] integrate multi-scale design into a single U-Net architecture, and, to the best of our knowledge, are the first to apply a frequency-domain loss function for deblurring. Instead of modifying the structure of U-Net, Chen et al. [12] introduce a building unit based on a gated architecture [16] and a squeeze-and-excitation block [27], resulting in an efficient and effective U-Net for deblurring tasks.

**Vision Transformers.** Recognizing the importance of global dependencies in high-level vision tasks, numerous vision Transformers (ViTs) have been developed for applications such as recognition [17, 62, 76], video and image classification [40, 41, 66], object detection [6, 85, 91], and semantic segmentation [59, 71, 90]. In low-level vision tasks, the high-resolution inputs make typical self-attention computationally costly. To address this, efficient variants such as W-MSA [37, 67], transposed self-attention [82], stripe and anchored stripe attention [36, 63], and frequency-based attention [31] have been developed. While these approaches reduce complexity from quadratic to linear, they often sacrifice key characteristics of standard self-attention. For example, W-MSA and stripe attention restrict the self-attention region, weakening global contextual representation, and frequency-based attention is mathematically closer to convolution than self-attention. In contrast to these methods, we introduce Concerto Self-Attention, a mechanism designed to capture both local and global relationships with linear complexity. Our approach achieves the highest PSNR and SSIM scores with relatively low FLOPs among deblurring Transformers.

## 3. Revisiting Self-Attention in Transformer

To better motivate our work, we begin by revisiting typical self-attention, W-MSA, and transposed self-attention. For typical self-attention, it first constructs *query*  $Q$ , *key*  $K$  and *value*  $V$  from the normalized tensor  $\mathbf{X} \in \mathbb{R}^{h \times w \times d}$  as follows:

$$Q = \mathbf{W}_p^q(\mathbf{X}), K = \mathbf{W}_p^k(\mathbf{X}), V = \mathbf{W}_p^v(\mathbf{X}), \quad (1)$$



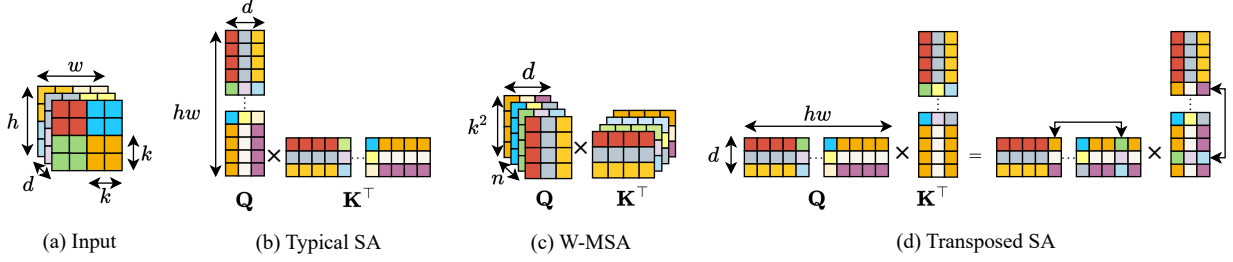


Figure 2. Self-attention methods. (a) Input tensor. (b) Typical self-attention. (c) Window multi-head self-attention [40, 41], where  $n = hw/k^2$  is the number of blocks. (d) Transposed self-attention [82] and a random column permutation. Column permutations do not affect the resulting attention map.

where  $Q, K, V \in \mathbb{R}^{hw \times d}$ ,  $\mathbf{W}_p^q$ ,  $\mathbf{W}_p^k$  and  $\mathbf{W}_p^v$  are linear projection operations. Then the self-attention is computed by:

$$\text{SA}(\mathbf{X}) = \text{softmax}(QK^\top/\sqrt{d})V, \quad (2)$$

where the  $\text{softmax}(\cdot)$  performs to the last dimension and  $d$  is the vector length of inner product.

Although the exhaustive calculation of self-attention yields satisfying results, the complexity is too high to be used for high-resolution images. W-MSA is proposed as an efficient substitute based on an intuitive assumption: Most large attention values are concentrated on the diagonal of an attention map because neighbor pixels are supposed to be highly correlated. W-MSA firstly divides the  $Q, K, V$  into  $k \times k$  non-overlapping blocks:  $Q_i, K_i, V_i \in \mathbb{R}^{k^2 \times d}$ , where  $1 \leq i \leq \frac{hw}{k^2} = n$ , and only calculates the self-attention within each block:

$$\text{W-MSA}(\mathbf{X})_i = \text{softmax}(Q_i K_i^\top/\sqrt{d})V_i. \quad (3)$$

As shown in Fig. 2(c), the self-attention between blocks (i.e., along the  $n$  axis) is overlooked. Fig. 4(b) provides another view of the resulting attention maps, where the attention outside the diagonal is omitted. W-MSA leaves out the relationships between blocks for efficiency.

Another way to reduce computational cost is to use the transposed operation [82], i.e.,  $\text{softmax}(Q^\top K)V^\top$ , to reduce the computational complexity from  $\mathcal{O}(h^2w^2)$  to  $\mathcal{O}(hw)$ . However, transposed self-attention lacks spatial awareness: random column permutations, or position swaps, do not make a difference to the resulting attention map, as shown in Fig. 2(d).

To overcome the problems mentioned above, we propose the *Concerto Self-Attention* (Section 4.1).

## 4. Proposed Method

In this section, we describe the design methodology of the proposed *Concertormer*, whose building block is composed of a Concerto Self-Attention module and a gated-dconv MLP. We first give an overview (see Fig. 3), and then thoroughly describe the CSA module in Section 4.1, the gdMLP

in Section 4.2 and implementation details in Section 4.3, respectively.

**Overall Architecture.** Fig. 3 shows the overall architecture on the left. We initially reduce its resolution by half using bilinear down-sampling to obtain  $\mathbf{I}_1 \in \mathbb{R}^{\frac{h}{2} \times \frac{w}{2} \times 3}$ , and similarly for  $\mathbf{I}_2 \in \mathbb{R}^{\frac{h}{4} \times \frac{w}{4} \times 3}$  and  $\mathbf{I}_3 \in \mathbb{R}^{\frac{h}{8} \times \frac{w}{8} \times 3}$ . The original blurry image  $\mathbf{I}_0$  and its down-sampled versions  $\mathbf{I}_1 - \mathbf{I}_3$  pass through a  $3 \times 3$  convolution layer to increase channel dimensions to  $1 \times, 2 \times, 3 \times$ , and  $4 \times$  the base width, respectively, before being fed to the encoders. In the decoders, a  $3 \times 3$  convolution layer with a skip connection to each input  $\mathbf{I}_0 - \mathbf{I}_3$  produces the output images of different scales, used in the loss function (Section 5.1). We replace traditional summation or concatenation between encoders and decoders with cross-attention (XA) on skip connections (see Section 4.3), and lower-resolution inputs are similarly fed to the encoders via XA. Within the encoders, the resolution is halved and channels are doubled using  $2 \times 2$  convolutions with stride 2, while in the decoders, resolution doubles, and channels halve using  $1 \times 1$  convolutions followed by pixel-shuffle [58]. Following [31, 82], block numbers increase from top to bottom in both encoders and decoders, with additional blocks allocated to the topmost decoder to refine the features before the final output.

### 4.1. Concerto Self-Attention

We propose a Concerto Self-Attention mechanism (see the right of Fig. 3) to reduce the time and space complexity of typical self-attention. The CSA prototype is defined as:

$$\text{CSA}(\mathbf{X})_i = (R_i + C)V_i, \quad (4a)$$

$$R_i = \text{softmax}\left(\frac{(Q_i K_i^\top - \overline{Q_i K_i^\top})}{\alpha}\right), \quad (4b)$$

$$C = \text{softmax}(\overline{Q_i K_i^\top}/\beta), \quad (4c)$$

where  $\overline{Q_i K_i^\top} = \sum_{i=1}^n Q_i K_i^\top / n$ ,  $\alpha$  and  $\beta$  are learnable scalars. The *Concertino* component  $C$  is applied to all  $V_i$ 's, computing the average attention across blocks to capture general spatial relationships, as shown in (4c). The *Ripieno* component  $R_i$ , specific to each  $V_i$ , represents the difference from the average and compensates for information loss.

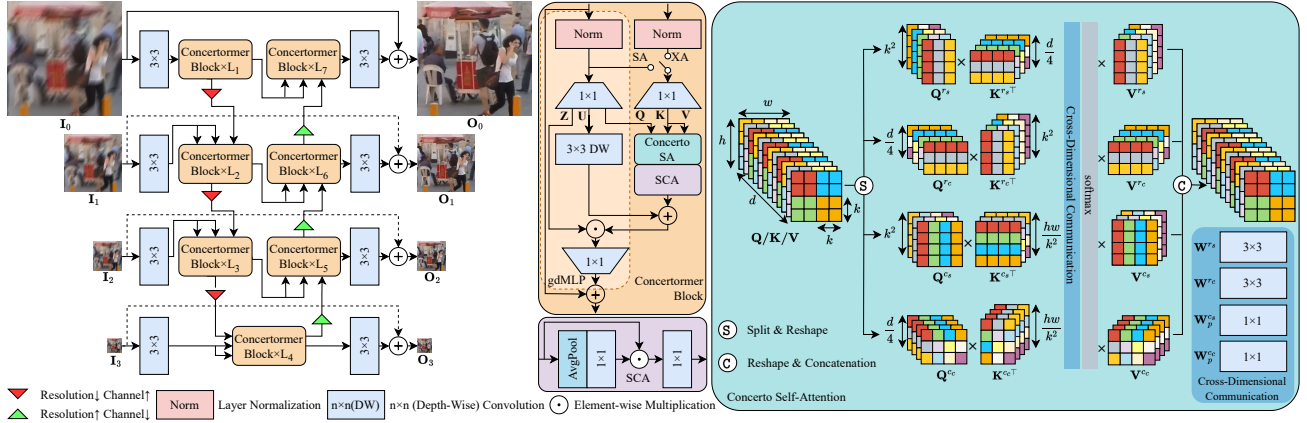


Figure 3. Network architecture. The overall network is shown on the left, and the sub-modules are on the right. XA: cross-attention, SA: self-attention. We use XA for the first blocks of  $L_2 - L_7$ , and SA for the remaining blocks.

To compute the CSA (4) efficiently, we divide the tensors into 2 parts, one for Concertino and one for Ripieno: we take  $Q_i^c, Q_i^r, K_i^c, K_i^r, V_i^c, V_i^r \in \mathbb{R}^{k^2 \times d_s/2}$  from  $Q_i, K_i, V_i$ , and compute the Ripieno and Concertino components as:

$$\text{CSA}(\mathbf{X}) = [\mathcal{R}V^r \quad \mathcal{C}V^c], \quad (5a)$$

$$\mathcal{R} = \text{diag}(R_1, \dots, R_n), \quad (5b)$$

$$\mathcal{C} = \text{diag}(C, \dots, C), \quad (5c)$$

$$R_i = \text{softmax} \left( (Q_i^r K_i^{r\top} - \overline{Q_i^r K_i^{r\top}}) / \alpha \right), \quad (5d)$$

$$C = \text{softmax} \left( \sum_i Q_i^c K_i^{c\top} / \beta \right), \quad (5e)$$

where  $V^r = [V_1^{r\top} \dots V_n^{r\top}]^\top$ ,  $V^c = [V_1^{c\top} \dots V_n^{c\top}]^\top$  and  $\text{diag}(\cdot)$  denotes a block diagonal matrix. Since a linear projection layer generally follows the self-attention module, we assume that the addition in (4a) can be absorbed to the projection layer and thus replaced with a concatenation operation in (5a), see Section 6.2 for further analysis. Additionally, by integrating the denominator  $n$  into the learnable  $\beta$ , we use summation in (5e) instead of average in (4c).

Note that (5e) can be expressed as follows:

$$\sum_i Q_i^c K_i^{c\top} = [Q_1^c \quad \dots \quad Q_n^c] \begin{bmatrix} K_1^{c\top} \\ \vdots \\ K_n^{c\top} \end{bmatrix} = Q^c K^{c\top}, \quad (6)$$

where  $Q^c, K^c \in \mathbb{R}^{k^2 \times \frac{d_s n}{2}}$ . Thus, (5e) can also be represented as a multiplication of two matrices.

Since the diagonal of (5b) can be regarded as a new dimension of the tensor, we express  $\mathcal{R}$  in a tensor  $\mathbf{R}^s \in \mathbb{R}^{n \times k^2 \times k^2}$ . To make the number of dimensions match, we choose  $\frac{d_s}{2}$  as the number of additional heads in (6). Thus, we have the tensor version of  $C$  as  $\mathbf{C}^s \in \mathbb{R}^{\frac{d_s}{2} \times k^2 \times k^2}$ . Then

(5b) and (5e) can be expressed as

$$\mathbf{R}^s = \text{softmax} \left( \mathbf{Q}^{r_s} \times \mathbf{K}^{r_s\top} - \overline{\mathbf{Q}^{r_s} \times \mathbf{K}^{r_s\top}} \right), \quad (7a)$$

$$\mathbf{C}^s = \text{softmax} \left( \mathbf{Q}^{c_s} \times \mathbf{K}^{c_s\top} \right), \quad (7b)$$

where  $\mathbf{Q}^{r_s}, \mathbf{K}^{r_s} \in \mathbb{R}^{t \times n \times k^2 \times \frac{d_s}{2}}$ ,  $\mathbf{Q}^{c_s}, \mathbf{K}^{c_s} \in \mathbb{R}^{t \times \frac{d_s}{2} \times k^2 \times n}$ ,  $t$  denotes the number of heads and  $\times$  the matrix multiplication of the last two dimensions. For simplicity, we omit the learnable scalars  $\alpha$  and  $\beta$  here and in the remaining parts of this paper. Fig. 4 illustrates the difference between CSA and typical SA and W-MSA in attention maps.

**Cross-Dimensional Communication.** In our CSA module, we have one more dimension, i.e.,  $n$  in (7a) and  $\frac{d_s}{2}$  in (7b), than the typical multi-head SA. Because the inner product is performed separately, we assume that building a connection between attention maps helps [56]. Thus, we propose the *Cross-Dimensional Communication* (CDC) to utilize the information across dimensions.

For Concertino tensor  $\mathbf{C}^s$ , the  $t \times \frac{d_s}{2}$  dimensions to be dealt with are constants, thus we use a  $t \times \frac{d_s}{2}$  to  $t \times \frac{d_s}{2}$  linear projection layer  $\mathbf{W}_p^{c_s}$ ; As for the Ripieno tensor  $\mathbf{R}^s$ , the dimension  $n = \frac{hw}{k^2}$  is varying according to the input size, thus a convolution substitutes for linear projection: we reshape the logits in (7a) to the size of  $t \times \frac{h}{k} \times \frac{w}{k} \times k^4$ , which is followed by a  $3 \times 3 \times 1$  convolutional layer  $\mathbf{W}^{r_s}$ , then reshape it back to the original shape. The Concerto Attention with CDC can be expressed as

$$\mathbf{R}^s = \text{softmax} \left( \mathbf{W}^{r_s} (\mathbf{Q}^{r_s} \times \mathbf{K}^{r_s\top}) \right), \quad (8a)$$

$$\mathbf{C}^s = \text{softmax} \left( \mathbf{W}_p^{c_s} (\mathbf{Q}^{c_s} \times \mathbf{K}^{c_s\top}) \right), \quad (8b)$$

where  $\mathbf{R}^s \in \mathbb{R}^{t \times n \times k^2 \times k^2}$ ,  $\mathbf{Q}^{r_s}, \mathbf{K}^{r_s} \in \mathbb{R}^{t \times n \times k^2 \times \frac{d_s}{2}}$ ,  $\mathbf{C}^s \in \mathbb{R}^{t \times \frac{d_s}{2} \times k^2 \times k^2}$  and  $\mathbf{Q}^{c_s}, \mathbf{K}^{c_s} \in \mathbb{R}^{t \times \frac{d_s}{2} \times k^2 \times n}$ . In (8a), we omit the mean  $\overline{Q_i^r K_i^{r\top}}$  as it is a linear combination of  $Q_i^r K_i^{r\top}$  and can be incorporated into  $\mathbf{W}^{r_s}$ . Additionally, via a convolutional layer, the global mean  $\overline{Q_i^r K_i^{r\top}}$  is

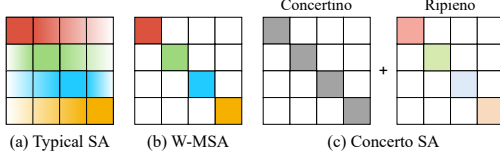


Figure 4. Attention maps. (a) Typical self-attention. The lighter color represents a smaller attention value. (b) Window multi-head self-attention (c) Concerto Self-Attention. Each block on the diagonal shares the same Concertino and has its own Ripieno component.

replaced by a local mean  $\sum_{j \in \mathcal{N}(i)} Q_j^r K_j^{r\top} / |\mathcal{N}(i)|$ , where  $\mathcal{N}(i)$  denotes the blocks covered by the convolutional kernel centered at  $i$ . Since Concertino  $\mathbf{C}^s$  already aggregates global information, the Ripieno  $\mathbf{R}^s$  can focus on local details, making the use of a local mean over  $\mathcal{N}(i)$  appropriate. See Section 6.2 for further analysis.

**Channel CSA.** Although the transposed self-attention [82] is computationally efficient, it does not model the spatial information well as shown in Section 3. To take advantage of complexity while ensuring that it can model spatial information well, we introduce the Concerto Self-Attention to the channel: taking  $Q_i^c, K_i^c, V_i^c \in \mathbb{R}^{d_c/2 \times k^2}$  from  $Q_i, K_i, V_i$ , we have similar results to (5), (6) and (8), except for  $Q^c, K^c \in \mathbb{R}^{\frac{d_c}{2} \times k^2 \times n}$ , where we choose  $k^2$  as the number of additional heads. The channel Concerto Self-Attention can be obtained by:

$$\mathbf{R}^c = \text{softmax}(\mathbf{W}^{r_c}(\mathbf{Q}^{r_c} \times \mathbf{K}^{r_c\top})), \quad (9a)$$

$$\mathbf{C}^c = \text{softmax}(\mathbf{W}^{c_c}(\mathbf{Q}^{c_c} \times \mathbf{K}^{c_c\top})), \quad (9b)$$

where  $\mathbf{R}^c \in \mathbb{R}^{t \times n \times \frac{d_c}{2} \times \frac{d_c}{2}}$  and  $\mathbf{C}^c \in \mathbb{R}^{t \times k^2 \times \frac{d_c}{2} \times \frac{d_c}{2}}$ . Since the position is separately recorded in the  $n$  dimension of  $\mathbf{R}^c$  and  $k^2$  of  $\mathbf{C}^c$ , our channel Concerto Self-Attention can sense spatial information.

**Mixing Projection.** Applying the Concerto Self-Attention to both spatial and channel dimension, we have  $\mathbf{X}^A = \mathbf{C}(\mathbf{R}^s \times \mathbf{V}^{r_s}, \mathbf{C}^s \times \mathbf{V}^{c_s}, \mathbf{R}^c \times \mathbf{V}^{r_c}, \mathbf{C}^c \times \mathbf{V}^{c_c})$ , where  $\mathbf{V}^{r_s} \in \mathbb{R}^{t \times n \times k^2 \times \frac{d_s}{2}}$ ,  $\mathbf{V}^{c_s} \in \mathbb{R}^{t \times \frac{d_s}{2} \times k^2 \times n}$ ,  $\mathbf{V}^{r_c} \in \mathbb{R}^{t \times n \times \frac{d_c}{2} \times k^2}$  and  $\mathbf{V}^{c_c} \in \mathbb{R}^{t \times k^2 \times \frac{d_c}{2} \times n}$ , and  $\mathbf{C}(\cdot)$  reshapes then concatenates tensors to  $\mathbb{R}^{h \times w \times d}$ .

Although these four attentions compute the spatial and channel relationships exhaustively, they are operated independently. Thus, we also use simplified channel attention (SCA) [12] to balance their importance. The SCA is defined as:

$$\text{SCA}(\mathbf{X}^A) = \mathbf{W}_p^2(\mathbf{W}_p^1(\text{AvgPool}(\mathbf{X}^A)) \odot_c \mathbf{X}^A), \quad (10)$$

where  $\odot_c$  denotes the channel-wise multiplication [27],  $\text{AvgPool}$  the global average pooling operation [38], and  $\mathbf{W}_p^1$  and  $\mathbf{W}_p^2$  are the functions of  $1 \times 1$  convolution. (10) is the final output of the Concerto Self-Attention module.

## 4.2. Gated-Dconv MLP

To reduce the complexity of the original Transformer FFN and enhance feature representation for image restoration, we propose the gated-dconv MLP, which works with the self-attention module within a single block (see the middle box of Fig. 3). The gdMLP can be expressed as

$$\text{gdMLP}(\mathbf{X}) = \mathbf{W}_p^g(\mathbf{U} \odot \mathbf{Z}), \quad (11a)$$

$$\mathbf{U} = \mathbf{W}_d^u(\mathbf{W}_p^u(\mathbf{X})), \quad (11b)$$

$$\mathbf{Z} = \mathbf{W}_p^z \mathbf{X}, \quad (11c)$$

where  $\odot$  denotes the element-wise product, and  $\mathbf{W}_d^U$  is the weight matrix of  $3 \times 3$  dconv;  $\mathbf{W}_p^u$ ,  $\mathbf{W}_p^z$  and  $\mathbf{W}_p^g$  are the weight matrices of  $1 \times 1$  convolution, respectively. To replace FFN, gdMLP has to incorporate the expansion-and-compression operation, so  $\mathbf{W}_p^z$  and  $\mathbf{W}_p^u$  double the channels and  $\mathbf{W}_p^g$  half the channels.

Unlike the gated MLP [39], we omit layer normalization and replace the spatial projection (a large linear layer for deblurring) with depth-wise convolution. This adjustment makes the module fully convolutional, which is efficiently suited for image restoration tasks.

To cooperate with the Concerto Self-Attention, as shown in Fig. 3, we modify (11a) as:

$$\text{gdMLP}(\mathbf{X}) = \mathbf{W}_p^g((\text{SCA}(\mathbf{X}^A) + \mathbf{U}) \odot \mathbf{Z}). \quad (12)$$

With the depth-wisely convolved tensor  $\mathbf{U}$ , the discontinuous border of non-overlapping blocks would be compensated.

## 4.3. Implementation Details

We choose the channel size  $d_s = d_c = \frac{d}{2t}$ , and block size  $k = 8$ . In the whole model, i.e., the left of Fig. 3, we apply the cross-attention mechanism to the first block in each level except for the topmost encoder. For the cross-attention blocks, whose  $\mathbf{K}$  and  $\mathbf{V}$  in (1) would be  $\mathbf{K} = \mathbf{W}_p^k(\mathbf{Y})$  and  $\mathbf{V} = \mathbf{W}_p^v(\mathbf{Y})$ , where  $\mathbf{Y}$  is the input other than  $\mathbf{X}$ . As shown in Fig. 3, the  $\mathbf{Y}$  of encoders comes from down-scaled inputs followed by a  $3 \times 3$  convolution; for decoders,  $\mathbf{Y}$  is the output of the encoder of the corresponding level.

We adopt multi-head attention in our models, where the number of heads increases with the channel number: the top encoder and decoder have a single head, and the layers beneath have double the heads of the above level.

*Concertormer* and *Concertormer-lite* both have channel width 48, which is the output channel size of the top left  $3 \times 3$  convolution on the left of fig. 3, and the expansion factor of gdMLP is set as 2, i.e., the channel numbers of  $\mathbf{W}_p^z$ ,  $\mathbf{W}_p^u$  in (11) and  $\mathbf{W}_p^q$ ,  $\mathbf{W}_p^k$ ,  $\mathbf{W}_p^v$  in (1) double the channels. The  $L_1$  to  $L_7$ , i.e., the block numbers shown in fig. 3, of *Concertormer-lite* are [4, 4, 12, 2, 12, 4, 4] and the full *Concertormer* [6, 8, 24, 2, 24, 8, 8].

Table 1. Results on the GOPRO [46] and HIDE [57] dataset, where our two models achieve the **best** and the **second-best** results.

Method	GOPRO		HIDE	
	PSNR	SSIM	PSNR	SSIM
DeblurGAN-v2 [32]	29.55	0.934	26.61	0.875
SRN [61]	30.26	0.934	28.36	0.904
DMPHN [83]	31.20	0.945	29.09	0.924
SAPHN [60]	31.85	0.948	29.98	0.930
MIMO-UNet+ [13]	32.45	0.957	29.99	0.930
MPRNet [81]	32.66	0.959	30.96	0.939
DeepRFT+ [43]	32.23	0.963	31.42	0.944
Restormer [82]	32.92	0.961	31.22	0.942
Uformer [67]	33.06	0.967	30.90	0.953
Stripformer [63]	33.08	0.962	31.22	0.942
MPRNet-local [14]	33.31	0.964	31.19	0.942
Restormer-local [14]	33.57	0.966	31.49	0.945
NAFNet [12]	33.71	0.967	31.32	0.943
GRL [36]	33.93	0.968	31.65	0.947
FFTformer [31]	<b>34.21</b>	0.969	31.62	0.946
DiffIR [69]	33.31	0.964	31.50	0.946
<i>Concertormer-lite</i>	34.18	<b>0.970</b>	<b>31.82</b>	<b>0.949</b>
<i>Concertormer</i>	<b>34.42</b>	<b>0.971</b>	<b>32.12</b>	<b>0.951</b>

## 5. Experimental Results

In this section, we first describe the datasets and training settings and compare our method with state-of-the-art ones in image deblurring. In addition, we show that our method can be applied to image draining and real image denoising.

### 5.1. Datasets and Training Details

Similarly to existing methods [13, 46, 81], we train our *Concertormer* on the GOPRO dataset, and evaluate it on GOPRO [46] and HIDE [57] for fairness. We also evaluate our method on the real-world deblurring datasets, i.e., REALBLUR-R and REALBLUR-J by [54]. We use the model trained on GOPRO and fine-tune it using the training data by [54].

For simplicity, we illustrate the training process for image deblurring on GOPRO; other tasks are detailed in the supplementary materials. We use  $\ell_1$  loss in the spatial domain and frequency domain as [13], where the ground-truth and its 3 down-sampled duplicates are used to calculate the loss between outputs  $O_0 - O_3$  in Fig. 3. As for training settings, we use AdamW [42] with  $\beta_1 = \beta_2 = 0.9$ , and weight decay of  $10^{-3}$ . Progressive training begins with  $128 \times 128$  patches and a batch size of 64, then scales to  $256 \times 256$  with batch size 16, and  $320 \times 320$  with batch size 8, each for 200,000 iterations. The learning rate starts at  $10^{-3}$ , decaying to  $10^{-7}$  via Cosine Annealing. The training patches are randomly cropped from  $512 \times 512$  overlapped patches and augmented by random flips and  $90^\circ$  rotations.

In addition to regular inference, we apply Test-time Local Converter (TLC) [14] during inference. The better results among the TLC inference and the regular inference are shown in this section.

### 5.2. Comparisons with State-of-the-Arts

**Evaluations on Synthetic Datasets.** Table 1 shows comparisons on the synthetic datasets GOPRO [46] and HIDE

Table 2. Results on the REALBLUR dataset [54].

Method	REALBLUR-R		REALBLUR-J	
	PSNR	SSIM	PSNR	SSIM
DeblurGAN-v2 [32]	35.11	0.935	28.69	0.866
SRN [61]	38.65	0.965	31.38	0.909
MIMO-UNet+ [13]	-	-	31.92	0.919
MAXIM-3S [65]	39.45	0.962	<b>32.84</b>	<b>0.935</b>
BANet [64]	39.55	0.971	32.00	0.923
DeepRFT+ [43]	39.70	0.971	32.18	0.928
Stripformer [63]	39.84	0.974	32.48	0.929
FMIMO-UNet+ [44]	39.98	0.973	32.56	0.932
FFTformer [31]	40.11	0.973	32.62	0.933
GRL [36]	<b>40.20</b>	<b>0.974</b>	32.82	0.932
<i>Concertormer</i>	<b>40.78</b>	<b>0.977</b>	<b>33.51</b>	<b>0.945</b>

Table 3. Image deblurring with JPEG artifacts.

Dataset	Metrics	MPRNet [81]	HiNet [11]	MAXIM [65]	NAFNet [12]	<i>Concertormer</i>
REDS-val-300 [47]	PSNR	28.79	28.83	28.93	<b>29.09</b>	<b>29.33</b>
	SSIM	0.811	0.862	0.865	<b>0.867</b>	<b>0.872</b>

Table 4. Image deraining results. We test on TEST100 [84], RAIN100H [74], RAIN100L [74], TEST2800 [19].

Method	TEST100		RAIN100H		RAIN100L		TEST2800		Average	
	PSNR	SSIM	PSNR	SSIM	PSNR	SSIM	PSNR	SSIM	PSNR	SSIM
DerainNet [81]	22.77	0.810	14.92	0.592	27.03	0.884	24.31	0.861	22.26	0.787
SEMI	22.35	0.788	16.56	0.486	25.03	0.842	24.43	0.782	22.09	0.725
DIDMDN	22.56	0.818	17.35	0.524	25.23	0.741	28.13	0.867	23.32	0.738
UMRL	24.41	0.829	26.01	0.832	29.18	0.923	29.97	0.905	27.39	0.872
RESCAN	25.00	0.835	26.36	0.786	29.80	0.881	31.29	0.904	28.11	0.852
PreNet	24.81	0.851	26.77	0.858	32.44	0.950	31.75	0.916	28.94	0.894
MSPFN	27.50	0.876	28.66	0.860	32.40	0.933	32.82	0.930	30.35	0.900
MPRNet	30.27	0.897	30.41	0.890	36.40	0.965	33.64	0.938	32.68	0.923
SPAIR	30.35	0.909	30.95	0.892	36.93	0.969	33.34	0.936	32.89	0.927
Restormer	<b>32.00</b>	<b>0.923</b>	<b>31.46</b>	<b>0.904</b>	<b>38.99</b>	<b>0.978</b>	<b>34.18</b>	<b>0.944</b>	<b>34.16</b>	<b>0.937</b>
<i>Concertormer</i>	<b>32.12</b>	<b>0.925</b>	<b>32.72</b>	<b>0.921</b>	<b>39.36</b>	<b>0.978</b>	<b>34.21</b>	<b>0.946</b>	<b>34.60</b>	<b>0.943</b>

[57]. Our models achieve the best and second-best results on these datasets. Compared to the FFTformer [31], our *Concertormer* further boosts the performance by 0.21 dB in terms of PSNR. Our lite model uses 16% fewer FLOPs while maintaining competitive performance, demonstrating the efficiency and effectiveness of *Concertormer* (Fig. 1).

Fig. 5 shows the visual comparisons on GOPRO: our model generates the fewest artifacts and the sharpest characters among these methods. We demonstrate the qualitative evaluation on HIDE in Fig. 6, where only our approach restores the eyes.

**Evaluations on Real-World Datasets.** Table 2 shows the deblurring results on the REALBLUR dataset. We compare our method to models trained or fine-tuned on REALBLUR, where our methods generate the highest PSNR and SSIM.

### 5.3. More Applications

We further show that our method can be applied to other related image restoration problems.

**Image Deblurring with JPEG Artifacts.** We train the model on REDS [47] and test on REDS-VAL-300 [11, 65]. Table 3 shows that *Concertormer* further boosts the performance by more than 0.2 dB in PSNR.

**Image Deraining.** Similar to [82], we train our model



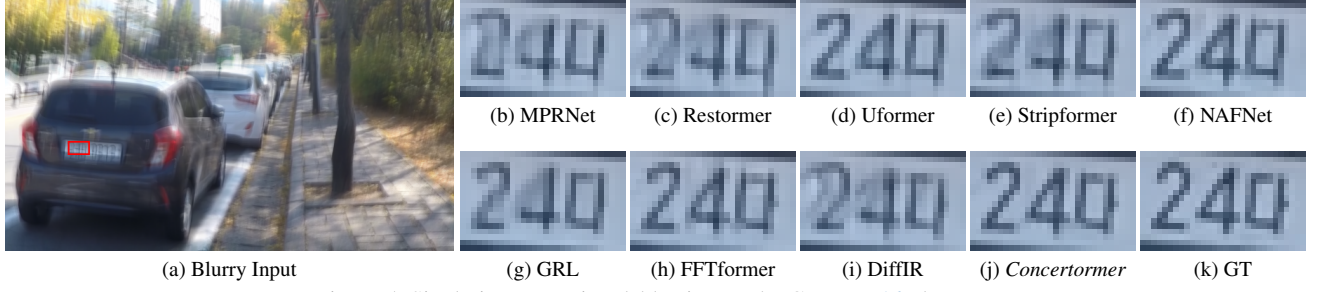


Figure 5. Single-image motion deblurring on the GoPro [46] dataset.

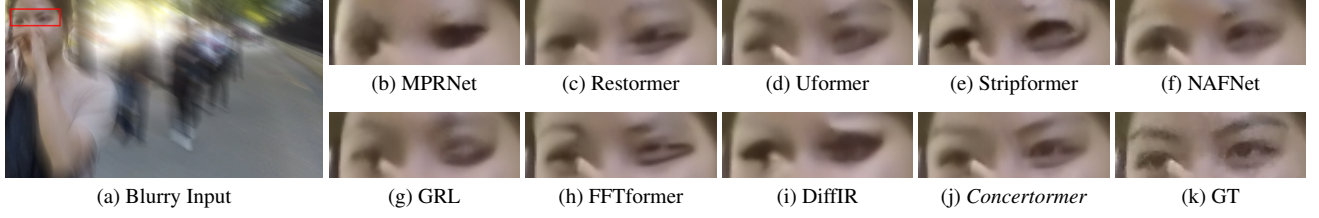


Figure 6. Single-image motion deblurring on the HIDE [57] dataset.

on RAIN13K [81] and test it on RAIN100H [70] and RAIN100L [70], TEST100 [84], and TEST2800 [19]. Following [28, 51, 81, 82], we compute evaluation metrics with Y channel of YCbCr color space. Table 4 shows that our method performs better on image deraining. Fig. 7 shows that *Concertormer* restores the images with better textures.

## 6. Analysis and Discussion

We have shown the effectiveness and efficiency of our method. This section analyzes the main components of *Concertormer* and the Concerto Self-Attention. The models in this section are constructed according to *Concertormer-lite* model, where the numbers of blocks  $L_1 - L_7$  are [4, 4, 12, 2, 12, 4, 4]. Patches of  $256 \times 256$  pixels of GoPro dataset and batch size 8 are used for 200,000 iterations, and the learning rate decreases from  $10^{-3}$  to  $10^{-6}$  by Cosine Annealing. FLOPs are computed via a  $256 \times 256$  input image. The other settings follow the formal *Concertormer* models described in Section 5.1.

### 6.1. Ablation Study

Table 5 shows the effect of each component, we modify the building blocks to examine the proposed method. These models are numbered for easier and clearer discussion: The study starts from a typical MLP (model 0); the Baseline (model 1) is the vanilla gdMLP without self-attention, and then we gradually add Concerto Self-Attention to gdMLP: the model 2 contains the self-attention mechanism of (8a) without  $\mathbf{W}^{rs}$ ; the model 3 contains (8) without  $\mathbf{W}^s$ ; the model 4 uses (9a) without  $\mathbf{W}^{rc}$  and model 5 uses (9) without  $\mathbf{W}^s$ ; model 6 uses the SA mechanisms of model 3 and model 5. Model 7 tests the effect of SCA (10), and the model 8 is the complete *Concertormer*.

The gdMLP architecture improves PSNR by over 6 dB

Table 5. Ablation study on the GoPro dataset. gdMLP: gated-conv MLP, FFN: Feed-Forward Network, SCA: simplified channel attention, MH: multi-head, CDC: Cross-Dimensional Communication,  $\mathbf{R}^s$ : spatial Ripieno  $\mathbf{C}^s$ : spatial Concertino,  $\mathbf{R}^c$ : channel Ripieno,  $\mathbf{C}^c$ : channel Concertino. The FLOPs are presented in Giga, and the parameters in Mega.

Model	Architecture		Concerto SA				SCA	CDC	Model Size		Metrics	
	FFN	gdMLP	$\mathbf{R}^s$	$\mathbf{C}^s$	$\mathbf{R}^c$	$\mathbf{C}^c$			FLOPs	Param	PSNR	SSIM
0	✓								52.87	11.0	26.28	0.851
1		✓							41.22	8.5	32.35	0.951
2		✓							119.34		32.58	0.953
3		✓	✓								33.11	0.958
4		✓				✓			155.38	21.2	32.65	0.953
5		✓			✓	✓			130.01		33.00	0.956
6		✓	✓	✓	✓	✓			118.33		33.20	0.958
7		✓	✓	✓	✓	✓	✓		118.57	26.3	33.31	0.959
8		✓	✓	✓	✓	✓	✓	✓	116.79	28.9	33.53	0.961
9	✓		✓	✓	✓	✓	✓	✓	116.81	29.2	31.90	0.945

while reducing FLOPs and parameters by more than 22% compared to the MLP. From model 2 to model 3, spatial CSA increases PSNR by over 0.5 dB, while channel CSA shows a 0.35 dB improvement (model 4 to model 5). For model 6, combining spatial and channel CSA boosts PSNR by about 0.85 dB over the Baseline. Model 7’s SCA adds 0.11 dB PSNR with simply 0.2% additional FLOPs. Finally, CDC enhances PSNR by 0.22 dB from model 7 to model 8. It is worth noting that, dividing channels for multiple self-attention mechanisms reduces FLOPs since the vector lengths for inner products are shortened, thereby the FLOPs decrease from model 4 to model 6. This further reduces the computational complexity of CSA.

To validate the effectiveness of the single-stage gdMLP architecture, we train a two-staged model combining Concerto Self-Attention and an FFN (model 9 in Table 5). With an adjusted FFN expansion factor to match the FLOPs and parameters of *Concertormer*, our method achieves higher PSNR by more than 1.6 dB.

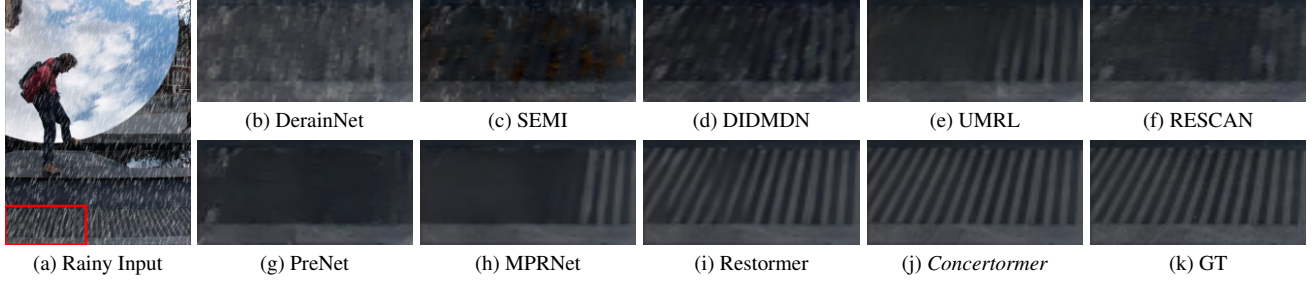


Figure 7. Deraining on the TEST100 [84] dataset.

## 6.2. Analysis of Concerto Self-Attention

We have shown the derivation of our method in Section 4.1, here we analyze how each step contributes to the satisfying results against the state-of-the-art works. In Table 6, we start from the Spatial Ripieno (model 2 in Table 5), which is the spatial fundamental model (i.e., (8a) without  $\mathbf{W}^{r_s}$ ). Then we implement and train the model of the Prototype (4), the Concerto Self-Attention (5), and CDC (8), respectively. To analyze our method better, we report the diffusion index (DI) in Table 6 and the local attribution maps (LAMs) in Fig. 8, where DI quantifies and LAM visualizes the receptive field [21], respectively.

Next, we analyze the models from (4) to (9) in Table 6. Comparing the Prototype to the Spatial Ripieno (model 2 of Table 5), although the PSNR and SSIM slightly decrease, the DI increases for about 32%. This suggests that the average operation in (4) significantly expands the receptive field with negligible additional computations. Fig. 8(b) and (c) show that the Prototype model extends self-attention to distant, correlated regions, such as the top-left corner. In the Concerto Self-Attention model, using concatenation in (5) instead of addition in (4) results in higher PSNR, SSIM, and DI, supporting the assumption that linear projection can replace addition. The bottom row of Table 6 shows the effect of the proposed CDC, which has the highest PSNR, SSIM, and DI at the cost of simply 0.36% more FLOPs and 6.13% more parameters. The largest receptive field in Fig. 8(f) also demonstrates the effect of the proposed CDC. We specifically validate our assumption in (8a), which allows us to omit the global mean. The result for “CDC w/ mean” includes the global mean, denoted as  $\mathbf{R}^s = \text{softmax}(\mathbf{W}^{r_s}(\mathbf{Q}^{r_s} \times \mathbf{K}^{r_s\top} - \mathbf{Q}^{r_s} \times \mathbf{K}^{r_s\top}))$ . We can note that the PSNR, SSIM, and DI are all getting lower with the global mean, and Fig. 8(e) demonstrates a smaller contribution area than Fig. 8(f).

To demonstrate the robustness and performance, we use the representative Restormer as our backbone and replace its transposed SA with Concerto Self-Attention, which is denoted as *Restormer\** in Table 7. We follow the training procedures and model configuration of the original Restormer for fair comparisons. With Concerto Self-Attention, *Restormer\** achieves an increase of 0.4 dB PSNR

Table 6. Influence of Concerto Self-Attention. We analyze the model size and metrics from Spatial Ripieno to our method step by step.

	Metrics			Model Size	
	PSNR	SSIM	DI	FLOPs(G)	Param(M)
Spatial Ripieno	32.58	0.953	20.51	119.34	21.2
Prototype	32.50	0.952	27.08		
Concerto	33.16	0.958	36.90		
CDC w/ mean	33.23	0.959	34.62	119.77	22.5
CDC	<b>33.30</b>	<b>0.960</b>	<b>39.15</b>		

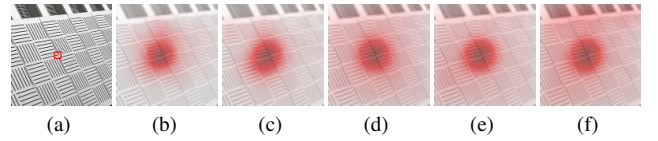


Figure 8. Comparison of local attribution maps [21]. (a) Ground truth and target patch. (b) - (f) Contribution areas of Spatial Ripieno, Prototype, Concerto Self-Attention, and CDC with and without global mean, respectively.

Table 7. Analysis of Concerto Self-Attention. The *Restormer\** model uses the CSA instead of transposed self-attention.

Method	GoPro [46]		HIDE [57]		Model Size	
	PSNR	SSIM	PSNR	SSIM	FLOPs(G)	Param(M)
Restormer [82]	32.92	0.961	31.22	0.942	140.99	26.1
<i>Restormer*</i>	<b>33.32</b>	<b>0.964</b>	<b>31.42</b>	<b>0.945</b>	140.29	31.0

on GoPro and 0.2 dB on HIDE with 0.5% lower FLOPs.

## 7. Conclusion

We introduce an efficient *Concertormer* that addresses a primary limitation in previous vision Transformers (ViTs): the trade-off between global contextual representation and computational complexity. The proposed Concerto Self-Attention mechanism captures both local and global connectivity across spatial and channel domains with linear complexity. Additionally, we propose a gated-dconv MLP, which consolidates the traditional two-staged Transformer architecture into a single stage. Experimental results demonstrate that the gdMLP with CSA performs favorably compared to the two-staged design at lower FLOPs. Replace the transposed self-attention with CSA, our method achieves higher PSNR at lower FLOPs compared to canonical Restormer. Beyond single-image motion deblurring, *Concertormer* also performs favorably in deblurring with JPEG artifacts and deraining.

## References

- [1] Abdelrahman Abdelhamed, Stephen Lin, and Michael S Brown. A high-quality denoising dataset for smartphone cameras. In *CVPR*, pages 1692–1700, 2018. 1
- [2] Abdullah Abuolaim and Michael S Brown. Defocus deblurring using dual-pixel data. In *ECCV*, pages 111–126. Springer, 2020. 2
- [3] Saeed Anwar and Nick Barnes. Real image denoising with feature attention. In *ICCV*, pages 3155–3164, 2019. 1
- [4] Saeed Anwar and Nick Barnes. Densely residual laplacian super-resolution. *IEEE TPAMI*, 44(3):1192–1204, 2020. 2
- [5] Yuanchao Bai, Gene Cheung, Xianming Liu, and Wen Gao. Graph-based blind image deblurring from a single photograph. *IEEE TIP*, 28(3):1404–1418, 2018. 2
- [6] Nicolas Carion, Francisco Massa, Gabriel Synnaeve, Nicolas Usunier, Alexander Kirillov, and Sergey Zagoruyko. End-to-end object detection with transformers. In *ECCV*, pages 213–229, 2020. 2
- [7] Meng Chang, Qi Li, Huajun Feng, and Zhihai Xu. Spatial-adaptive network for single image denoising. In *ECCV*, pages 171–187. Springer, 2020. 1
- [8] Hanting Chen, Yunhe Wang, Tianyu Guo, Chang Xu, Yiping Deng, Zhenhua Liu, Siwei Ma, Chunjing Xu, Chao Xu, and Wen Gao. Pre-trained image processing transformer. In *CVPR*, pages 12299–12310, 2021. 1
- [9] Liang Chen, Faming Fang, Tingting Wang, and Guixu Zhang. Blind image deblurring with local maximum gradient prior. In *CVPR*, pages 1742–1750, 2019. 2
- [10] Liang Chen, Faming Fang, Shen Lei, Fang Li, and Guixu Zhang. Enhanced sparse model for blind deblurring. In *ECCV*, pages 631–646. Springer, 2020. 2
- [11] Liangyu Chen, Xin Lu, Jie Zhang, Xiaojie Chu, and Chengpeng Chen. Hinet: Half instance normalization network for image restoration. In *CVPR*, pages 182–192, 2021. 6, 7, 8
- [12] Liangyu Chen, Xiaojie Chu, Xiangyu Zhang, and Jian Sun. Simple baselines for image restoration. In *ECCV*, pages 17–33. Springer, 2022. 2, 5, 6, 1, 7, 8
- [13] Sung-Jin Cho, Seo-Won Ji, Jun-Pyo Hong, Seung-Won Jung, and Sung-Jea Ko. Rethinking coarse-to-fine approach in single image deblurring. In *ICCV*, pages 4641–4650, 2021. 2, 6
- [14] Xiaojie Chu, Liangyu Chen, Chengpeng Chen, and Xin Lu. Improving image restoration by revisiting global information aggregation. In *ECCV*, pages 53–71. Springer, 2022. 6
- [15] Kostadin Dabov, Alessandro Foi, Vladimir Katkovnik, and Karen Egiazarian. Image denoising by sparse 3-d transform-domain collaborative filtering. *IEEE TIP*, 16(8):2080–2095, 2007. 1
- [16] Yann N Dauphin, Angela Fan, Michael Auli, and David Grangier. Language modeling with gated convolutional networks. In *ICML*, pages 933–941. PMLR, 2017. 2
- [17] Alexey Dosovitskiy, Lucas Beyer, Alexander Kolesnikov, Dirk Weissenborn, Xiaohua Zhai, Thomas Unterthiner, Mostafa Dehghani, Matthias Minderer, Georg Heigold, Sylvain Gelly, et al. An image is worth 16x16 words: Transformers for image recognition at scale. *ICLR*, 2021. 2
- [18] Xueyang Fu, Jiabin Huang, Xinghao Ding, Yinghao Liao, and John Paisley. Clearing the skies: A deep network architecture for single-image rain removal. *IEEE TIP*, 26(6):2944–2956, 2017. 8, 9
- [19] Xueyang Fu, Jiabin Huang, Delu Zeng, Yue Huang, Xinghao Ding, and John Paisley. Removing rain from single images via a deep detail network. In *CVPR*, pages 3855–3863, 2017. 6, 7
- [20] Mor Geva, Roei Schuster, Jonathan Berant, and Omer Levy. Transformer feed-forward layers are key-value memories. *arXiv:2012.14913*, 2020. 2
- [21] Jinjin Gu and Chao Dong. Interpreting super-resolution networks with local attribution maps. In *CVPR*, pages 9199–9208, 2021. 8
- [22] Shi Guo, Zifei Yan, Kai Zhang, Wangmeng Zuo, and Lei Zhang. Toward convolutional blind denoising of real photographs. In *CVPR*, pages 1712–1722, 2019. 1
- [23] Dafang He, Xiao Yang, Chen Liang, Zihan Zhou, Alexander G Ororbi, Daniel Kifer, and C Lee Giles. Multi-scale fcn with cascaded instance aware segmentation for arbitrary oriented word spotting in the wild. In *CVPR*, pages 3519–3528, 2017. 2
- [24] Kaiming He, Jian Sun, and Xiaoou Tang. Single image haze removal using dark channel prior. *IEEE TPAMI*, 33(12):2341–2353, 2010. 2
- [25] Kaiming He, Xiangyu Zhang, Shaoqing Ren, and Jian Sun. Deep residual learning for image recognition. In *CVPR*, pages 770–778, 2016. 2
- [26] Hexiang Hu, Shiyi Lan, Yuning Jiang, Zhimin Cao, and Fei Sha. Fastmask: Segment multi-scale object candidates in one shot. In *CVPR*, pages 991–999, 2017. 2
- [27] Jie Hu, Li Shen, and Gang Sun. Squeeze-and-excitation networks. In *CVPR*, pages 7132–7141, 2018. 2, 5
- [28] Kui Jiang, Zhongyuan Wang, Peng Yi, Chen Chen, Baojin Huang, Yimin Luo, Jiayi Ma, and Junjun Jiang. Multi-scale progressive fusion network for single image deraining. In *CVPR*, pages 8346–8355, 2020. 7
- [29] Yoonsik Kim, Jae Woong Soh, Gu Yong Park, and Nam Ik Cho. Transfer learning from synthetic to real-noise denoising with adaptive instance normalization. In *CVPR*, pages 3482–3492, 2020. 1
- [30] Goro Kobayashi, Tatsuki Kuribayashi, Sho Yokoi, and Kentaro Inui. Analyzing feed-forward blocks in transformers through the lens of attention map. In *ICLR*, 2024. 2
- [31] Lingshun Kong, Jiangxin Dong, Jianjun Ge, Mingqiang Li, and Jinshan Pan. Efficient frequency domain-based transformers for high-quality image deblurring. In *CVPR*, pages 5886–5895, 2023. 2, 3, 6, 4, 5, 7
- [32] Orest Kupyn, Tetiana Martyniuk, Junru Wu, and Zhangyang Wang. Deblurgan-v2: Deblurring (orders-of-magnitude) faster and better. In *ICCV*, pages 8878–8887, 2019. 2, 6, 4, 5, 7
- [33] Wei-Sheng Lai, Jia-Bin Huang, Narendra Ahuja, and Ming-Hsuan Yang. Deep laplacian pyramid networks for fast and accurate super-resolution. In *CVPR*, pages 624–632, 2017. 2
- [34] Wei-Sheng Lai, Jia-Bin Huang, Narendra Ahuja, and Ming-Hsuan Yang. Fast and accurate image super-resolution with



- deep laplacian pyramid networks. *IEEE TPAMI*, 41(11): 2599–2613, 2018. 2
- [35] Xia Li, Jianlong Wu, Zhouchen Lin, Hong Liu, and Hongbin Zha. Recurrent squeeze-and-excitation context aggregation net for single image deraining. In *ECCV*, pages 254–269, 2018. 8, 9
- [36] Yawei Li, Yuchen Fan, Xiaoyu Xiang, Denis Demandolx, Rakesh Ranjan, Radu Timofte, and Luc Van Gool. Efficient and explicit modelling of image hierarchies for image restoration. In *CVPR*, pages 18278–18289, 2023. 2, 6, 3, 4, 5, 7
- [37] Jingyun Liang, Jiezhong Cao, Guolei Sun, Kai Zhang, Luc Van Gool, and Radu Timofte. Swinir: Image restoration using swin transformer. In *ICCV Workshops*, pages 1833–1844, 2021. 1, 2
- [38] Min Lin, Qiang Chen, and Shuicheng Yan. Network in network. *arXiv:1312.4400*, 2013. 5
- [39] Hanxiao Liu, Zihang Dai, David So, and Quoc V Le. Pay attention to mlp. *NIPS*, 34:9204–9215, 2021. 2, 5
- [40] Ze Liu, Yutong Lin, Yue Cao, Han Hu, Yixuan Wei, Zheng Zhang, Stephen Lin, and Baining Guo. Swin transformer: Hierarchical vision transformer using shifted windows. In *ICCV*, pages 10012–10022, 2021. 2, 3
- [41] Ze Liu, Han Hu, Yutong Lin, Zhuliang Yao, Zhenda Xie, Yixuan Wei, Jia Ning, Yue Cao, Zheng Zhang, Li Dong, et al. Swin transformer v2: Scaling up capacity and resolution. In *CVPR*, pages 12009–12019, 2022. 2, 3
- [42] Ilya Loshchilov and Frank Hutter. Decoupled weight decay regularization. *arXiv:1711.05101*, 2017. 6
- [43] Xintian Mao, Yiming Liu, Wei Shen, Qingli Li, and Yan Wang. Deep residual fourier transformation for single image deblurring. *arXiv:2111.11745*, 2021. 6, 4, 5, 7
- [44] Xintian Mao, Yiming Liu, Fengze Liu, Qingli Li, Wei Shen, and Yan Wang. Intriguing findings of frequency selection for image deblurring. In *AAAI*, pages 1905–1913, 2023. 6, 4, 5, 7
- [45] Chong Mou, Jian Zhang, and Zhuoyuan Wu. Dynamic attentive graph learning for image restoration. In *ICCV*, pages 4328–4337, 2021. 1
- [46] Seungjun Nah, Tae Hyun Kim, and Kyoung Mu Lee. Deep multi-scale convolutional neural network for dynamic scene deblurring. In *CVPR*, pages 3883–3891, 2017. 2, 6, 7, 8, 3
- [47] Seungjun Nah, Sanghyun Son, Suyoung Lee, Radu Timofte, and Kyoung Mu Lee. Ntire 2021 challenge on image deblurring. In *CVPR*, pages 149–165, 2021. 6, 7, 8
- [48] Jinshan Pan, Zhouchen Lin, Zhixun Su, and Ming-Hsuan Yang. Robust kernel estimation with outliers handling for image deblurring. In *CVPR*, pages 2800–2808, 2016. 2
- [49] Jinshan Pan, Deqing Sun, Hanspeter Pfister, and Ming-Hsuan Yang. Blind image deblurring using dark channel prior. In *CVPR*, pages 1628–1636, 2016. 2
- [50] Jinsun Park, Yu-Wing Tai, Donghyeon Cho, and In So Kweon. A unified approach of multi-scale deep and hand-crafted features for defocus estimation. In *CVPR*, pages 1736–1745, 2017. 2
- [51] Kuldeep Purohit, Maitreya Suin, AN Rajagopalan, and Vishnu Naresh Boddeti. Spatially-adaptive image restoration using distortion-guided networks. In *CVPR*, pages 2309–2319, 2021. 7
- [52] Chao Ren, Xiaohai He, Chunheng Wang, and Zhibo Zhao. Adaptive consistency prior based deep network for image denoising. In *CVPR*, pages 8596–8606, 2021. 1
- [53] Dongwei Ren, Wangmeng Zuo, Qinghua Hu, Pengfei Zhu, and Deyu Meng. Progressive image deraining networks: A better and simpler baseline. In *CVPR*, pages 3937–3946, 2019. 8, 9
- [54] Jaesung Rim, Haeyun Lee, Jucheol Won, and Sunghyun Cho. Real-world blur dataset for learning and benchmarking deblurring algorithms. In *ECCV*, pages 184–201. Springer, 2020. 6, 4, 5, 7
- [55] Olaf Ronneberger, Philipp Fischer, and Thomas Brox. U-net: Convolutional networks for biomedical image segmentation. In *MICCAI*, pages 234–241. Springer, 2015. 2
- [56] Noam Shazeer, Zhenzhong Lan, Youlong Cheng, Nan Ding, and Le Hou. Talking-heads attention. *arXiv:2003.02436*, 2020. 4
- [57] Ziyi Shen, Wenguan Wang, Xiankai Lu, Jianbing Shen, Haibin Ling, Tingfa Xu, and Ling Shao. Human-aware motion deblurring. In *ICCV*, pages 5572–5581, 2019. 1, 6, 7, 8, 3, 4
- [58] Wenzhe Shi, Jose Caballero, Ferenc Huszar, Johannes Totz, Andrew P Aitken, Rob Bishop, Daniel Rueckert, and Zehan Wang. Real-time single image and video super-resolution using an efficient sub-pixel convolutional neural network. In *CVPR*, pages 1874–1883, 2016. 3
- [59] Robin Strudel, Ricardo Garcia, Ivan Laptev, and Cordelia Schmid. Segmenter: Transformer for semantic segmentation. In *ICCV*, pages 7262–7272, 2021. 2
- [60] Maitreya Suin, Kuldeep Purohit, and AN Rajagopalan. Spatially-attentive patch-hierarchical network for adaptive motion deblurring. In *CVPR*, pages 3606–3615, 2020. 6
- [61] Xin Tao, Hongyun Gao, Xiaoyong Shen, Jue Wang, and Ji-aya Jia. Scale-recurrent network for deep image deblurring. In *CVPR*, pages 8174–8182, 2018. 2, 6
- [62] Hugo Touvron, Matthieu Cord, Matthijs Douze, Francisco Massa, Alexandre Sablayrolles, and Hervé Jégou. Training data-efficient image transformers & distillation through attention. In *ICML*, pages 10347–10357. PMLR, 2021. 2
- [63] Fu-Jen Tsai, Yan-Tsung Peng, Yen-Yu Lin, Chung-Chi Tsai, and Chia-Wen Lin. Stripformer: Strip transformer for fast image deblurring. In *ECCV*, pages 146–162. Springer, 2022. 2, 6, 3, 4, 5, 7
- [64] Fu-Jen Tsai, Yan-Tsung Peng, Chung-Chi Tsai, Yen-Yu Lin, and Chia-Wen Lin. Banet: a blur-aware attention network for dynamic scene deblurring. *IEEE TIP*, 31:6789–6799, 2022. 6
- [65] Zhengzhong Tu, Hossein Talebi, Han Zhang, Feng Yang, Peyman Milanfar, Alan Bovik, and Yinxiao Li. Maxim: Multi-axis mlp for image processing. In *CVPR*, pages 5769–5780, 2022. 6, 4, 5, 7
- [66] Xiaolong Wang, Ross Girshick, Abhinav Gupta, and Kaiming He. Non-local neural networks. In *CVPR*, pages 7794–7803, 2018. 2



- [67] Zhendong Wang, Xiaodong Cun, Jianmin Bao, Wengang Zhou, Jianzhuang Liu, and Houqiang Li. Uformer: A general u-shaped transformer for image restoration. In *CVPR*, pages 17683–17693, 2022. 1, 2, 6, 3, 4
- [68] Wei Wei, Deyu Meng, Qian Zhao, Zongben Xu, and Ying Wu. Semi-supervised transfer learning for image rain removal. In *CVPR*, pages 3877–3886, 2019. 8, 9
- [69] Bin Xia, Yulun Zhang, Shiyin Wang, Yitong Wang, Xinglong Wu, Yapeng Tian, Wenming Yang, and Luc Van Gool. Diffir: Efficient diffusion model for image restoration. In *ICCV*, pages 13095–13105, 2023. 6, 2, 3, 4
- [70] Li Xu, Shicheng Zheng, and Jiaya Jia. Unnatural l0 sparse representation for natural image deblurring. In *CVPR*, pages 1107–1114, 2013. 7
- [71] Lian Xu, Wanli Ouyang, Mohammed Bennamoun, Farid Boussaid, and Dan Xu. Multi-class token transformer for weakly supervised semantic segmentation. In *CVPR*, pages 4310–4319, 2022. 2
- [72] Yanyang Yan, Wenqi Ren, Yuanfang Guo, Rui Wang, and Xiaochun Cao. Image deblurring via extreme channels prior. In *CVPR*, pages 4003–4011, 2017. 2
- [73] Chao Yang, Xin Lu, Zhe Lin, Eli Shechtman, Oliver Wang, and Hao Li. High-resolution image inpainting using multi-scale neural patch synthesis. In *CVPR*, pages 6721–6729, 2017. 2
- [74] Wenhan Yang, Robby T Tan, Jiashi Feng, Jiaying Liu, Zongming Guo, and Shuicheng Yan. Deep joint rain detection and removal from a single image. In *CVPR*, pages 1357–1366, 2017. 6, 9
- [75] Rajeev Yasarla and Vishal M Patel. Uncertainty guided multi-scale residual learning-using a cycle spinning cnn for single image de-raining. In *CVPR*, pages 8405–8414, 2019. 8, 9
- [76] Li Yuan, Yunpeng Chen, Tao Wang, Weihao Yu, Yujun Shi, Zi-Hang Jiang, Francis EH Tay, Jiashi Feng, and Shuicheng Yan. Tokens-to-token vit: Training vision transformers from scratch on imagenet. In *ICCV*, pages 558–567, 2021. 2
- [77] Zongsheng Yue, Hongwei Yong, Qian Zhao, Deyu Meng, and Lei Zhang. Variational denoising network: Toward blind noise modeling and removal. *NIPS*, 32, 2019. 1
- [78] Zongsheng Yue, Qian Zhao, Lei Zhang, and Deyu Meng. Dual adversarial network: Toward real-world noise removal and noise generation. In *ECCV*, pages 41–58. Springer, 2020. 1
- [79] Syed Waqas Zamir, Aditya Arora, Salman Khan, Munawar Hayat, Fahad Shahbaz Khan, Ming-Hsuan Yang, and Ling Shao. Cycleisp: Real image restoration via improved data synthesis. In *CVPR*, pages 2696–2705, 2020. 1
- [80] Syed Waqas Zamir, Aditya Arora, Salman Khan, Munawar Hayat, Fahad Shahbaz Khan, Ming-Hsuan Yang, and Ling Shao. Learning enriched features for real image restoration and enhancement. In *ECCV*, pages 492–511. Springer, 2020. 2, 1
- [81] Syed Waqas Zamir, Aditya Arora, Salman Khan, Munawar Hayat, Fahad Shahbaz Khan, Ming-Hsuan Yang, and Ling Shao. Multi-stage progressive image restoration. In *CVPR*, pages 14821–14831, 2021. 2, 6, 7, 1, 3, 4, 8, 9
- [82] Syed Waqas Zamir, Aditya Arora, Salman Khan, Munawar Hayat, Fahad Shahbaz Khan, and Ming-Hsuan Yang. Restormer: Efficient transformer for high-resolution image restoration. In *CVPR*, pages 5728–5739, 2022. 1, 2, 3, 5, 6, 7, 8, 4, 9
- [83] Hongguang Zhang, Yuchao Dai, Hongdong Li, and Piotr Koniusz. Deep stacked hierarchical multi-patch network for image deblurring. In *CVPR*, pages 5978–5986, 2019. 2, 6
- [84] He Zhang, Vishwanath Sindagi, and Vishal M Patel. Image de-raining using a conditional generative adversarial network. *IEEE TCSVT*, 30(11):3943–3956, 2019. 6, 7, 8
- [85] Jing Zhang, Jianwen Xie, Nick Barnes, and Ping Li. Learning generative vision transformer with energy-based latent space for saliency prediction. *NIPS*, 34:15448–15463, 2021. 2
- [86] Kai Zhang, Wangmeng Zuo, Yunjin Chen, Deyu Meng, and Lei Zhang. Beyond a gaussian denoiser: Residual learning of deep cnn for image denoising. *IEEE TIP*, 26(7):3142–3155, 2017. 1
- [87] Kai Zhang, Yawei Li, Wangmeng Zuo, Lei Zhang, Luc Van Gool, and Radu Timofte. Plug-and-play image restoration with deep denoiser prior. *IEEE TPAMI*, 44(10):6360–6376, 2021. 2
- [88] Yulun Zhang, Kunpeng Li, Kai Li, Lichen Wang, Bineng Zhong, and Yun Fu. Image super-resolution using very deep residual channel attention networks. In *ECCV*, pages 286–301, 2018. 2
- [89] Yulun Zhang, Yapeng Tian, Yu Kong, Bineng Zhong, and Yun Fu. Residual dense network for image restoration. *IEEE TPAMI*, 43(7):2480–2495, 2020. 2
- [90] Sixiao Zheng, Jiachen Lu, Hengshuang Zhao, Xiatian Zhu, Zekun Luo, Yabiao Wang, Yanwei Fu, Jianfeng Feng, Tao Xiang, Philip HS Torr, et al. Rethinking semantic segmentation from a sequence-to-sequence perspective with transformers. In *CVPR*, pages 6881–6890, 2021. 2
- [91] Xizhou Zhu, Weijie Su, Lewei Lu, Bin Li, Xiaogang Wang, and Jifeng Dai. Deformable detr: Deformable transformers for end-to-end object detection. *arXiv:2010.04159*, 2020. 2

# Efficient Concertormer for Image Deblurring and Beyond

## Supplementary Material

In this supplemental material, we first provide real noisy image denoising results and discuss limitations. Then we report training details of tasks other than single-image motion deblurring. Finally, we provide more visual comparisons.

### 8. Evaluations on Real Noisy Image Denoising

We further evaluate our method on the real noisy image denoising on the SIDD dataset. Table 8 shows that the proposed methods, i.e., *Concertormer* and *Concertormer*<sup>†</sup><sup>1</sup>, achieve comparable performance against state-of-the-art ones.

### 9. Limitation Analysis

We have demonstrated the efficiency of *Concertormer* in the main paper. Although we propose a building block that can be applied to existing restoration models to solve kinds of image restoration tasks, the backbone restoration model still requires a careful design for better performance improvement when using the proposed *Concertormer*. For example, the improvement of the proposed method on image denoising is marginal as shown in Table 8.

Table 8. Real noisy image denoising. \* denotes methods using additional training data. *Concertormer*<sup>†</sup> has more blocks in the latent layer.

Dataset	Metrics	DnCNN [86]	BM3D [15]	CBDNet* [22]	RIDNet* [3]	AINDNet* [29]	VDN [77]	SADNet* [7]	DANet+* [78]	CycleISP* [79]	MIRNet [80]	DeamNet* [52]	MPRNet [81]	DAGL [45]	Uformer [67]	Restormer [82]	NAFNet [12]	<i>Concertormer</i>	<i>Concertormer</i> <sup>†</sup>
SIDD [1]	PSNR	23.66	25.65	30.78	38.71	38.95	39.28	39.46	39.47	39.52	39.72	39.35	39.71	38.94	39.77	40.02	40.30	40.28	40.32
	SSIM	0.583	0.685	0.801	0.951	0.952	0.956	0.957	0.957	0.957	0.959	0.955	0.958	0.953	0.959	0.960	0.962	0.962	0.962

### 10. Other Training Details

For real noisy image denoising on the SIDD dataset, we train the model for 400,000 iterations, following [12], as additional iterations do not yield further improvements. Since both the training and testing data consist of  $256 \times 256$  pixel images, we do not employ progressive training; instead, we train the model exclusively on  $256 \times 256$  patches.

For the deraining task, however, we adopt a progressive training strategy. The model is trained with  $192 \times 192$  patches for 100,000 iterations, followed by  $256 \times 256$  patches for 200,000 iterations,  $320 \times 320$  patches for 100,000 iterations, and an additional 10,000 iterations using  $128 \times 128$  patches.

As for REDS, we train the model as described in Section 5.1 with the configuration as Section 4.3.

### 11. More Visual Comparisons

<sup>1</sup>The architecture of *Concertormer* is detailed in Section 4.3, while for *Concertormer*<sup>†</sup>, the configuration of  $L_1 - L_7$  is [2, 4, 8, 16, 8, 4, 4].



Figure 9. Visual comparisons of single-image motion deblurring on GoPRO [46].

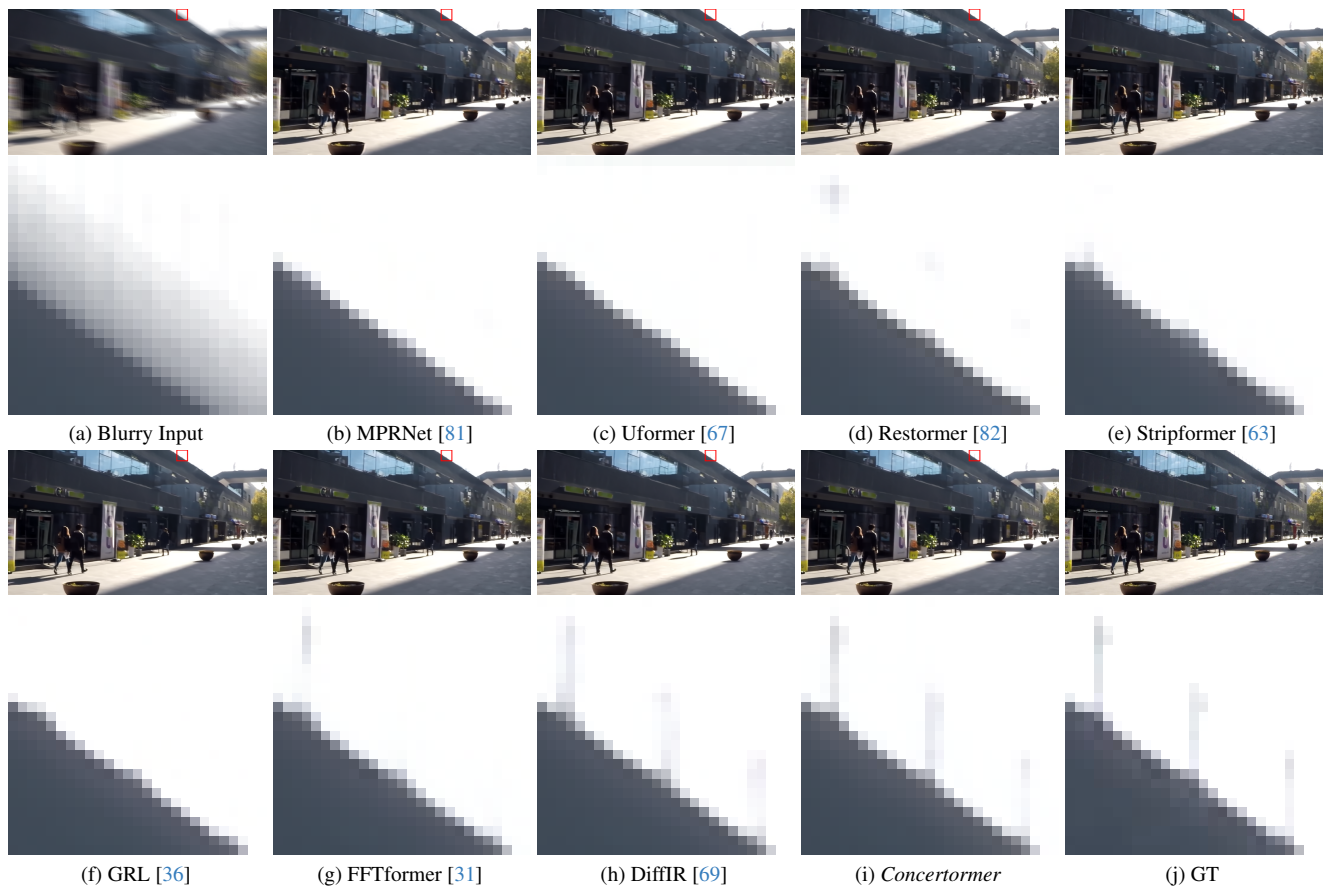


Figure 10. Visual comparisons of single-image motion deblurring on GOPRO [46].



Figure 11. Visual comparisons of single-image motion deblurring on HIDE [57].





Figure 12. Visual comparisons of single-image motion deblurring on HIDE [57].

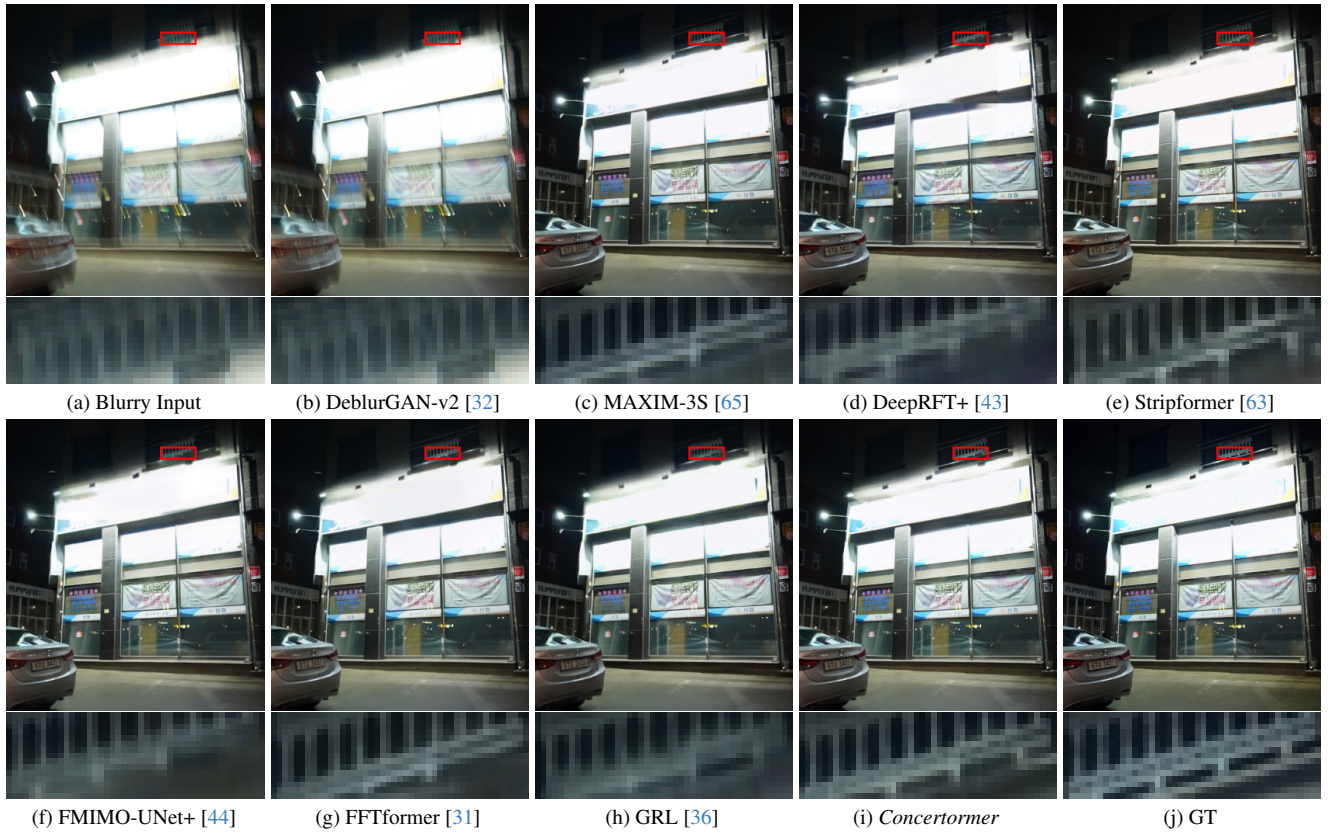


Figure 13. Visual comparisons of single-image motion deblurring on REALBLUR.J [54].

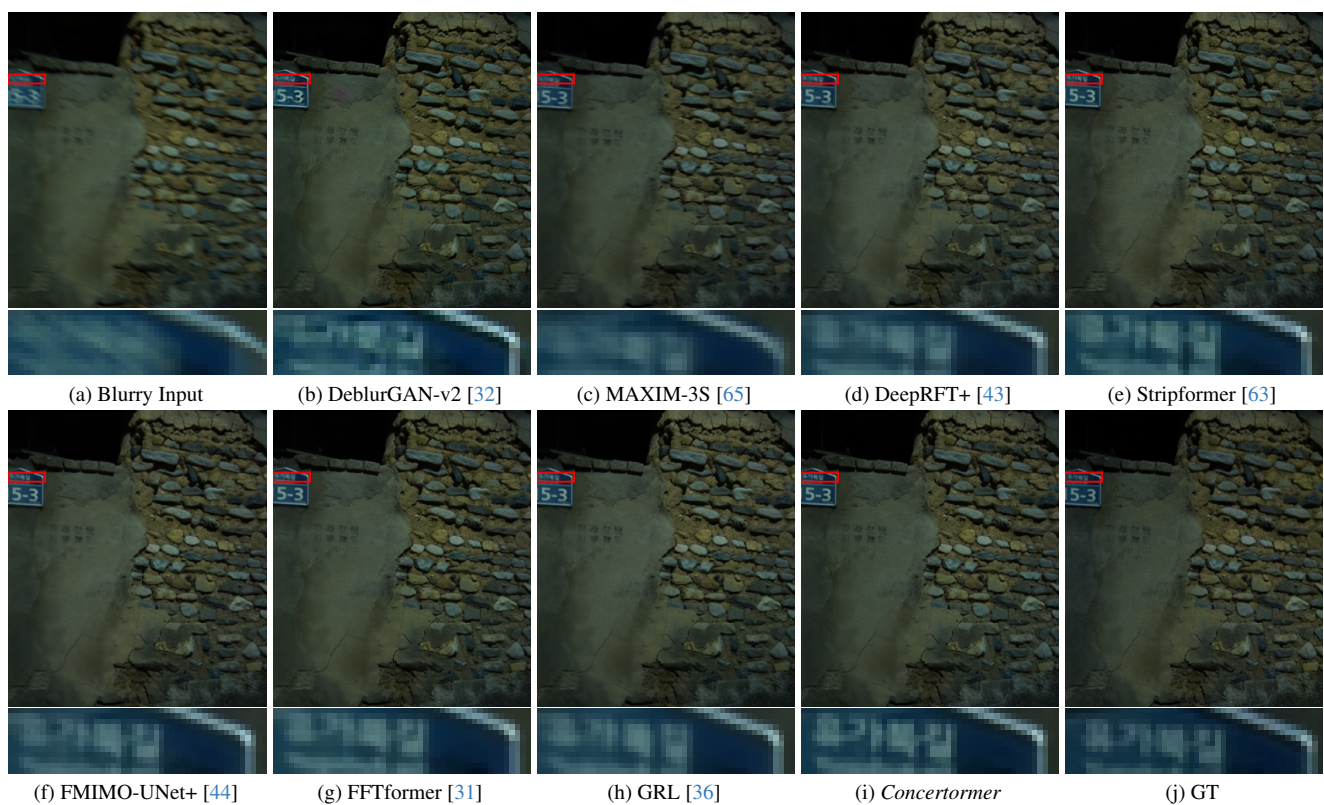


Figure 14. Visual comparisons of single-image motion deblurring on REALBLUR.J [54].



Figure 15. Visual comparisons of single-image motion deblurring on REALBLUR-J [54].



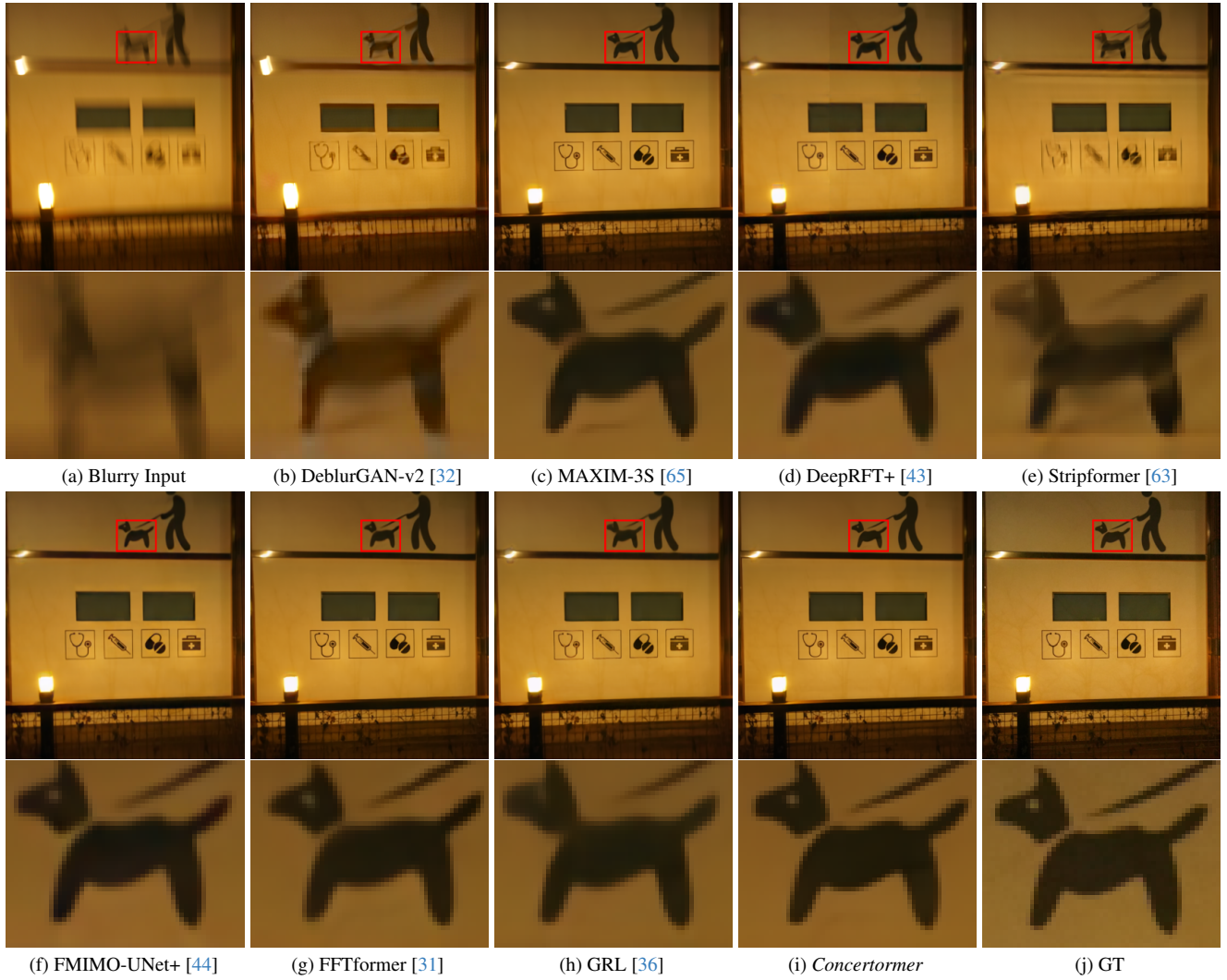


Figure 16. Visual comparisons of single-image motion deblurring on REALBLUR\_J [54].

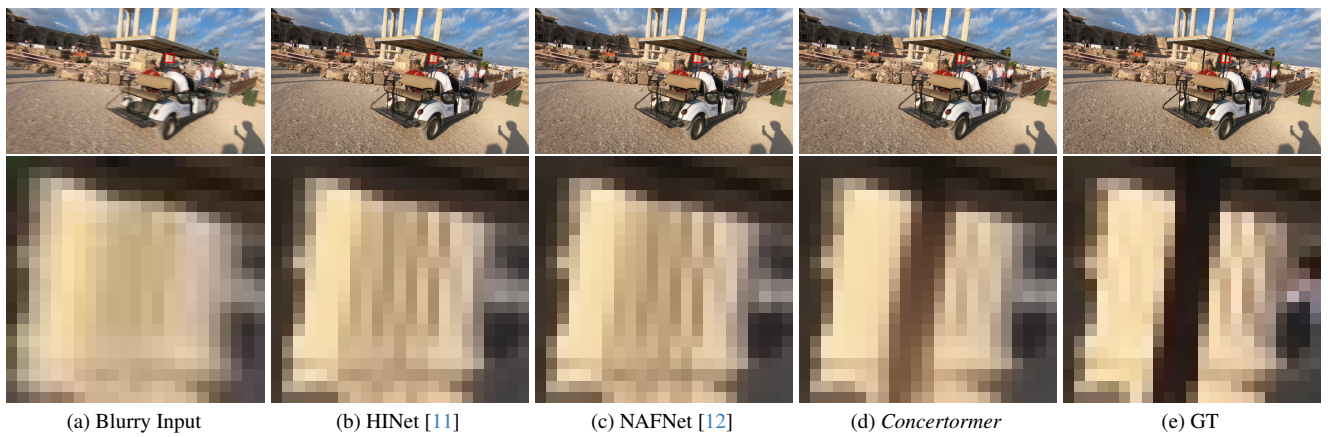


Figure 17. Visual comparisons of motion deblurring with JPEG artifacts on REDS-val-300 [47].



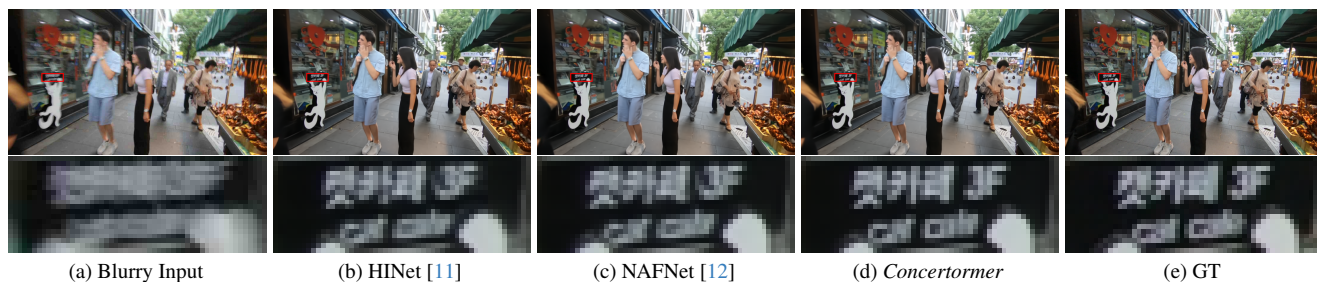


Figure 18. Visual comparisons of motion deblurring with JPEG artifacts on REDS-val-300 [47].

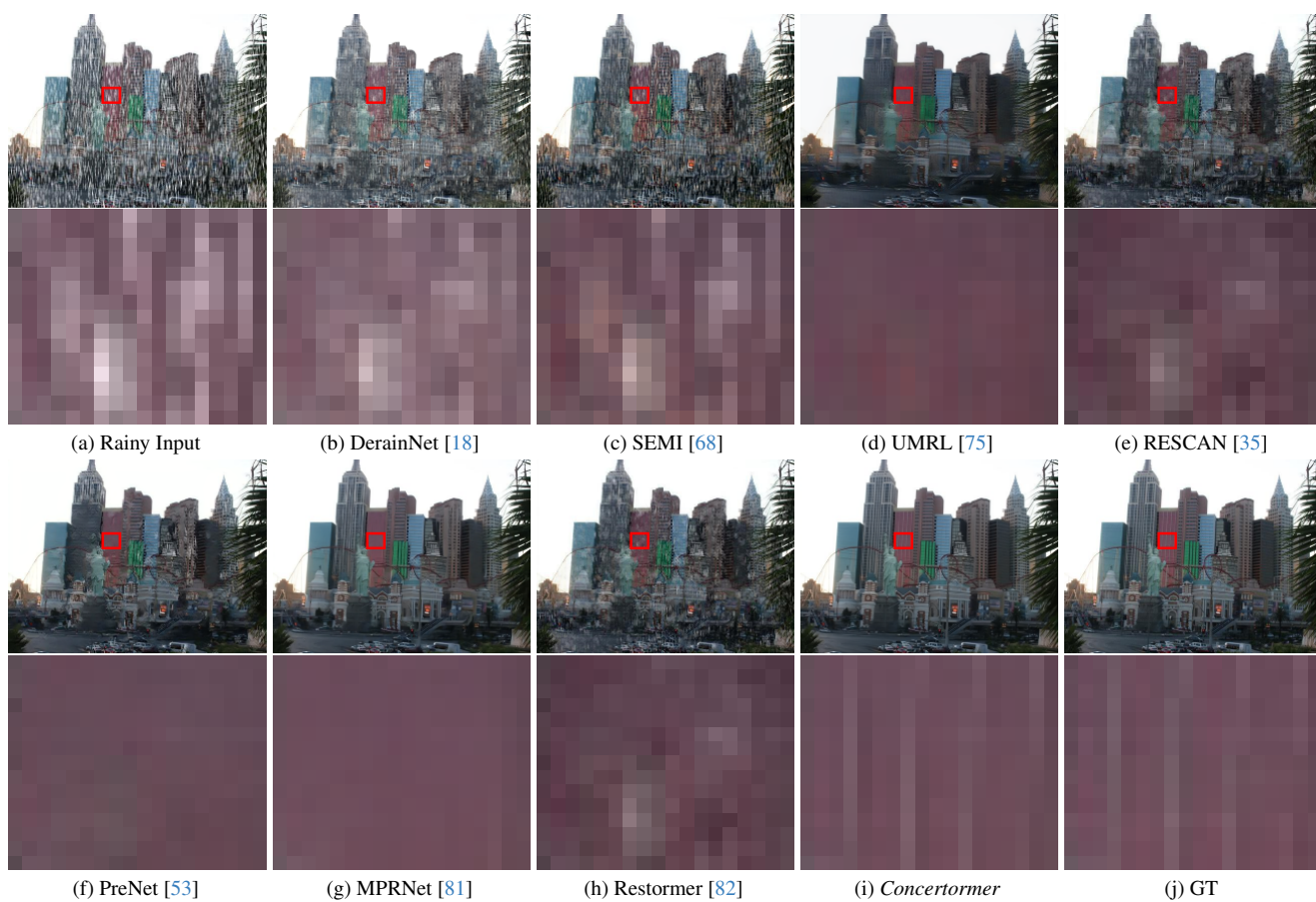


Figure 19. Visual comparisons of deraining on TEST100 [84].

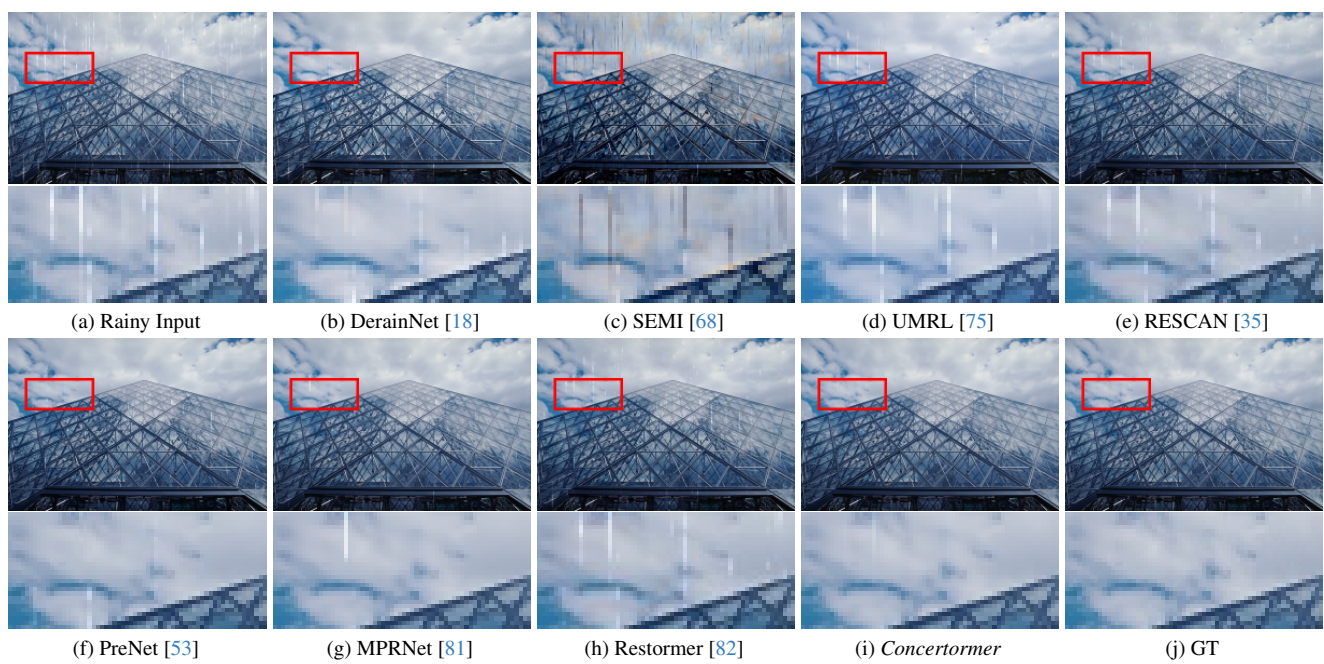


Figure 20. Visual comparisons of deraining on RAIN100L [74].